

Article

Internal Dynamic Temperature Measurement of Alkali Metal Vapor Cell by Kalman Filter

Yang Li ¹, Shencheng Tian ¹, Junpeng Zhao ², Guoqing Zhou ¹, Xiangmei Dong ¹, Xiumin Gao ¹ and Xuejing Liu ^{1,*}

¹ School of Optical-Electrical and Computer Engineering, University of Shanghai for Science and Technology, Shanghai 200093, China

² Beijing Institute of Space Launch Technology, Beijing 100076, China

* Correspondence: liuxuejing@usst.edu.cn

Abstract: Measuring the internal dynamic temperature of alkali metal vapor cells is crucial for enhancing the performance of numerous atomic devices. However, conventional methods of measuring the internal dynamic temperature of the cell are prone to errors. To obtain a more accurate internal dynamic temperature of the alkali metal vapor cell, a temperature measuring method based on the data fusion of the Kalman filter has been proposed. This method combines the indirect temperature measurement signal from a resistance temperature detector with the atomic absorption spectrometric temperature measurement signal. This provides a high-accuracy set of internal dynamic temperatures in the cell. The atomic vapor density calculated from the final fusion results is 37% average lower than that measured by external wall temperature measurements, which is in line with the conclusions reached in many previous studies. This study is highly beneficial to measure the temperature of alkali metal vapor cells.

Keywords: alkali metal vapor cell; atomic devices; atomic absorption spectrometry (AAS); Kalman filter (KF); data fusion



Citation: Li, Y.; Tian, S.; Zhao, J.; Zhou, G.; Dong, X.; Gao, X.; Liu, X. Internal Dynamic Temperature Measurement of Alkali Metal Vapor Cell by Kalman Filter. *Photonics* **2023**, *10*, 492. <https://doi.org/10.3390/photonics10050492>

Received: 27 March 2023

Revised: 19 April 2023

Accepted: 21 April 2023

Published: 24 April 2023



Copyright: © 2023 by the authors. Licensee MDPI, Basel, Switzerland. This article is an open access article distributed under the terms and conditions of the Creative Commons Attribution (CC BY) license (<https://creativecommons.org/licenses/by/4.0/>).

1. Introduction

A cell containing one or more alkali metals, inert and buffer vapors, is commonly used as a core device in atomic clocks [1], laser stabilizers [2], and optical magnetometers [3–7]. In magnetic field detection, spin-exchange-free spin (SERF) atomic magnetometers are highly valued for their ultra-high sensitivity. SERF atomic magnetometers are now widely used in biomedical [8,9] and geomagnetic exploration [10] fields. The density of alkali metal vapor in the cell is closely related to its temperature. Alcock's [11] formula for the saturation vapor pressure of alkali metals can be used to calculate the temperature. The density of alkali metal vapor significantly affects the optical depth of the cell medium, atomic polarization, atomic relaxation rate, and other factors. Therefore, exploring the internal dynamic temperature of the alkali metal cell is important.

Traditional temperature measurement of the cell involves installing a resistance temperature detector (RTD) on the outer wall of the cell, which is non-destructive [12]. However, this method has limitations. This is because the saturated vapor pressure of the cell is determined by the lowest temperature point of the entire cell, but the external temperature of the cell is not consistent, making it difficult to find the lowest temperature point of the alkali metal cell.

To address this problem many scholars have studied methods for cell temperature measurement. Shang et al. [13] used atomic absorption spectrometry (AAS) to obtain the internal temperature of the cell, which is more accurate than using RTD. Meanwhile, many scholars have found that the atomic vapor density obtained by RTD temperature using Killian's formula is much higher than the true atomic vapor density. Shao et al. [14] measured the density of alkali metal vapor, which is about half of the result calculated by the Killian formula; Shang et al. [15] come to the same conclusion based on the measurement of

alkali metal vapor density using the Faraday modulator. The reason for this phenomenon is currently unknown, but obtaining the true temperature inside the cell is an area worth exploring.

The methods for measuring the temperature of the cell are divided into two types: contact and non-contact. The non-contact measurement method is based on AAS. It offers high sensitivity, calibration-free operation, fast detection, and the ability to remotely measure the internal dynamic temperature inside the cell without entering the cell [15]. Therefore, the AAS temperature measurement method is beneficial for measuring the temperature inside the cell. RTDs have high measurement accuracy and stable performance, which is suitable for measuring temperature signals. Therefore, RTD-based temperature measurement is also suitable for measuring the temperature of cells. However, both temperature measurement methods have technical drawbacks that are hard to avoid. Measurements using RTDs require additional calculations to obtain the temperature at the center of the cell. Hence, temperature measurements using this method are inaccurate. AAS temperature measurement utilizes fitting absorption spectra, but measurement becomes challenging when the vapor density is high. This is because directly measuring the extremely weak transmitted light near resonance is difficult. Moreover, severe attenuation of light within the resonance linewidth makes it hard to determine the absorption line shape, which makes it impossible to measure through far detuned measurement [16]. Additionally, AAS measurement is affected by factors such as power fluctuations and changes in external magnetic fields. As a result, AAS may not be an accurate method for temperature measurement [17]. In this study, the results of indirect temperature measurement by RTD, temperature measurement by AAS, and direct temperature measurement of the external wall by RTD are compared. This study has found that measured temperatures vary greatly, especially during periods of increased internal dynamic temperature. The dynamic internal temperature of the cell requires a high precision measurement, but the results obtained from different temperature measurement methods may vary. Measuring the internal dynamic temperature of a cell requires high accuracy. For this purpose, a method of fusing data from two temperature measurement devices is used to measure the internal dynamic temperature of the cell. This multimodal sensor-data fusion method allows more accurate measurements [18]. Multi-sensor data fusion is useful when the measured temperature by a single sensor does not have the desired precision. So, the data from multiple sensors is processed to compensate for the individual sensor's deficiencies [19]. The data fusion methods are mainly divided into two types: modern and classical fusion methods. The modern fusion methods are based on neural networks [20], cluster analysis [21], and intelligent algorithms [22]. The classical fusion methods revolve around the Kalman filter (KF) [23] and Bayesian estimation [24].

Many research studies have been done on the KF data fusion method. Sun et al. [25] proposed an optimal information fusion dispersion KF for multiple sensors and verified the effectiveness of the method with a three-sensor radar tracking system. Wang et al. [26] fused the signals from lead-zirconium-titanium oxide (PZT) sensors and optical fiber sensors for monitoring bore edge cracks through a weighted adaptive KF. They found that the method could significantly improve the accuracy compared to single-sensor monitoring. Xu et al. [27] used KF to fuse resolution-enhanced surface temperature data with coarse-resolution surface temperature data to obtain a more accurate set of surface temperatures with a root mean square error in the range from 0.79–1.47 K. Chen et al. [28] proposed a KF-based algorithm to fuse temperature and humidity data. The experimental results showed that the algorithm filtered the data noise, reduced the data measurement error, and obtained highly accurate values.

The KF is used to fuse the measurement data from multimodal sensors. The KF acquires accurate data by combining the model state estimation with the observed data [29]. It can obtain a better set of measurements for the same object. In this study, the KF is used to measure the more accurate internal dynamic temperature of the cell. It is done by fusing correlated time series data of AAS and RTD.

The structure of this article is as follows. Firstly, the acquisition of the external wall temperature data of the vapor cell and the AAS measurement data related to the internal dynamic temperature of the cell is presented. Afterward, the data processing of the internal dynamic temperature of the cell is discussed. Next, the calculation of the internal dynamic temperature of the cell through KF data fusion for a more accurate internal dynamic temperature of the cell is done. Finally, the fusion results are compared with the external wall measurements of RTD to verify the KF fusion results. In the end, it is shown, based on the experimental results, that it is feasible to measure the internal dynamic temperature of the cell with multiple sensor data after processing with KF.

2. Measurement Procedures

2.1. AAS Temperature Measurement

Due to the lack of hyperfine pumping, hyperfine absorption is completely overlapped. Hence, the optical depth of the target can be measured according to the change in light intensity. The schematic diagram of the AAS setup is shown in Figure 1. Based on Lambert’s law, the relationship between the corresponding quantities is presented in Equation (1) [30]:

$$I(O) = I(I) \exp(-OD) = I(I) \exp(-\rho \cdot l \cdot s) \tag{1}$$

where $I(I)$ is the light intensity of the laser incident on the cell, $I(O)$ is the light intensity of the laser exiting the cell, OD is the optical depth, ρ is the atomic density of the alkali metal vapor, s is the photon absorption cross-section, and l is the optical length of the laser beam in the cell.

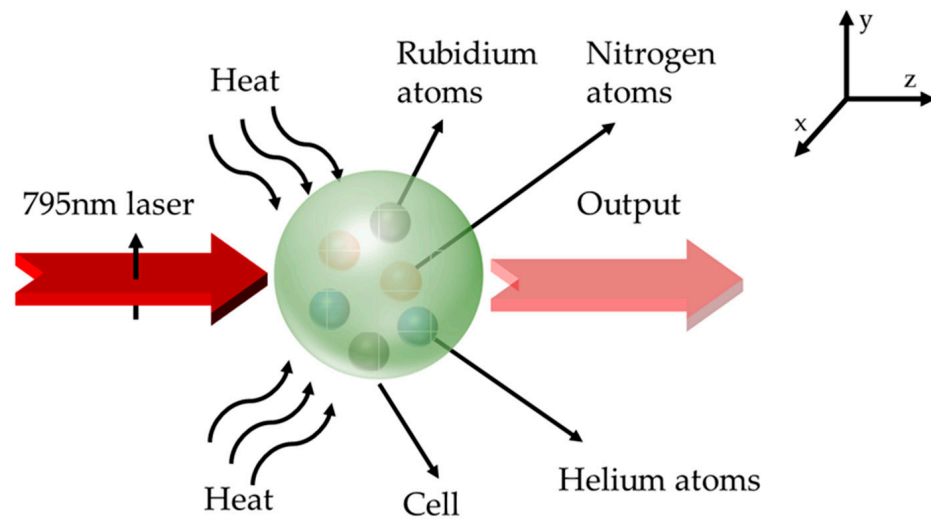


Figure 1. The schematic diagram of AAS setup. A 795 nm laser beam enters the heated cell with a light intensity $I(I)$, gets absorbed and exits the cell with a light intensity $I(O)$.

The buffer gas atom causes a linear Lorentz broadening between atoms. To avoid collision relaxation, the cell used in the experiment injects three atmospheres of ^4He . Under these conditions, an approximate broadening of 50 GHz is observed, and saturated absorption peaks were not visible. Consequently, based on a known set of measurement data, the single peak Lorentz function in Equation (2) is capable of fitting the data [31]. The fitting results are then used to calculate the full width at half maximum (FWHM) Γ , the center frequency ν_0 .

$$L(\nu - \nu_0) = \frac{\Gamma / (2\pi)}{(\nu - \nu_0)^2 + (\Gamma / 2)^2} \tag{2}$$

Substituting Γ of the curve into Equation (3) representing the absorption area at the resonant frequency point, the photon absorption cross-sectional area $s(\nu)$ can be calculated as follows [32].

$$s(\nu) = \pi r_e c f \cdot L(\nu - \nu_0) \tag{3}$$

In Equation (3), r_e is the electron radius, c is the speed of light in vacuum, and f is the intensity of the oscillator. The atomic density n of alkali metal vapor is obtained through Equation (4), where OD_{max} is the maximum optical depth, $s(\nu_0) = s_{max}$ is the maximum photon absorption cross-sectional area at resonance [33]:

$$\rho = \frac{OD_{max}}{s_{max} l} \tag{4}$$

The empirical formula given in Equation (5) presents the relationship between cell temperature and the atomic density of alkali metal vapor [11,13]:

$$\rho = \frac{1}{T_G} 10^{A - \frac{B}{T_G}} \tag{5}$$

Equation (5) provides the cell temperature T_G if all the other quantities are known. A and B are the density parameters of liquid rubidium (Rb) vapor with the following values $A = 31.178$ and $B = 4040$.

2.2. RTD Indirect Temperature Measurement

The RTD temperature measurement method is invasive, which means that it needs to be in direct contact with the object being measured. However, because the cell is non-destructive and the RTD is pre-installed during cell manufacturing, the RTD may be corroded by alkali metal vapor. As a result, RTD can only measure the temperature of the outer wall of the cell.

According to Fourier’s law of heat conduction, heat will move from a high temperature region to a low temperature region when there is non-uniform temperature distribution. Equation (5) indicates that the temperature of the cell is directly proportional to the atomic density of alkali metal vapor. The electric heating plate is in close contact with the cell while it is being charged and heated. The lack of internal heating in the cell results in a slight gradient of temperature along its radius. Thus, the external wall of the cell with a radius of 10 mm can be simulated as being in a state of thermal equilibrium. In the transient case of 428 K, the cell is simulated in two dimensions. In the two-dimensional case, the temperature distribution in the cell is approximated by the two-dimensional Gaussian distribution model shown in Figure 2. Therefore, in this work, a simplified temperature distribution model is proposed, in which the temperature distribution of the cell is considered to have an inverse Gaussian function.

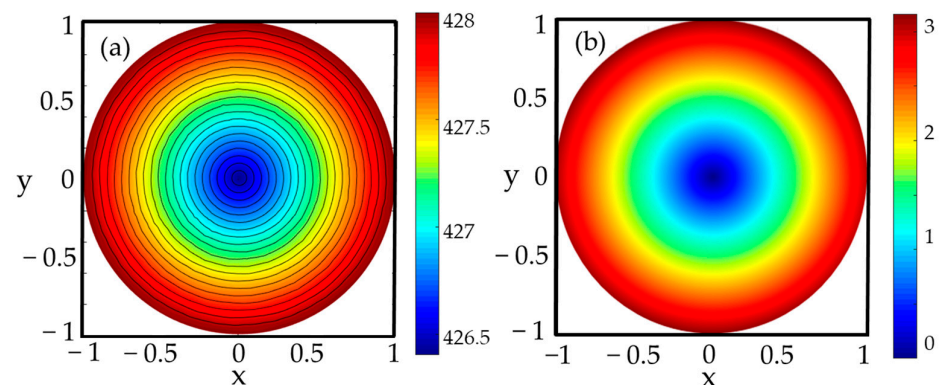


Figure 2. Cell temperature model. (a) The simulation plot, and (b) the cone distribution plot.

This article describes a simple simulation of the constant temperature situation in the 428 K cell, as shown in Figure 2a. In this case, the temperature of the cell has reached a steady state. We treat the cell wall as a constant temperature heat source, regardless of the temperature exchange between the cell and the environment.

Thus, the isotherms of the cell can be simplified into regular circles. When measured outside the cell, the extended isotherms of the heat source at any point are perpendicular to the heat transfer and, as a result, must pass through the center of the spherical cell. Additionally, assuming that heat transfer comes from an infinite number of equivalent heat sources, a way to estimate cell temperature from the temperature of the outer wall is provided.

The concentration of alkali metal vapor in the cell is determined by the point where the alkali condenses at low temperatures. However, Guo et al. [34] found that the distribution of alkali metal vapor within the cell is not uniform, and the reason for this is not fully understood. Therefore, let's consider Equation (1) and assume that the object has the same atomic density at the same temperature. In the full optical range, there are i optical lengths of varying density, and each optical length with the same density is considered a unit length. By substituting these variables in Equation (1), we can express the attenuation coefficient of laser light passing through the cell as $\lambda_1, \lambda_2, \lambda_3 \dots \lambda_i$, and the corresponding optical length as $l_1, l_2, l_3 \dots l_i$. The following expression is obtained:

$$\lambda_1 l_1 + \lambda_2 l_2 + \lambda_3 l_3 + \dots + \lambda_i l_i = \ln\left(\frac{I(I)}{I(O)}\right) \tag{6}$$

The internal distribution of alkali metal vapor in the heating cell is not uneven. From Equations (4) and (5) it is clear that temperature, optical depth, and alkali metal vapor density are positively correlated. Therefore, the variation of the attenuation coefficient is also distributed in the inverted Gaussian function. Hence, Equation (7) can be used to represent the optical depth of the medium within a certain range. l_a and l_b are the lower and upper limits within the cell.

$$\int_{l_a}^{l_b} \lambda(x, y) dl = OD' \tag{7}$$

Substituting this value in Equations (4) and (5) gives the temperature T_D at a point in the interval.

2.3. KF Fusion Algorithm

The KF is a recursive optimization algorithm whose main application is in time-varying dynamic systems with uncertainty [25]. It is difficult to establish an accurate mathematical model of the internal dynamic temperature of a cell. Whether the internal dynamic temperature of the cell is extrapolated from RTD measurements or measured by AAS, there will always be unmeasurable errors. Therefore, the use of a KF for data fusion is very appropriate.

The spatial state system model of the object under test can be expressed as:

$$x(k + 1) = Ax(k) + w(k) \tag{8}$$

$$y(k) = Hx(k) + v(k) \tag{9}$$

where $x(k)$ is the state matrix of the object under observation at the moment k . $y(k)$ is the state observation signal of the object under test at the moment k . $w(k)$ is the process noise at the moment k . $v(k)$ is the observation noise at the moment k . A and H are the state transfer matrix and the observation matrix, respectively. Both $w(k)$ and $v(k)$ are Gaussian white noises, and their corresponding covariance matrices are Q and R . The core formula for the KF is as follows [28].

State space projections:

$$x(k|k-1) = Ax(k-1) \tag{10}$$

$$P(k|k-1) = AP(k-1)A^T + Q \tag{11}$$

Updated state space:

$$K(k) = P(k|k-1)H^T [HP(k|k-1)H^T + R]^{-1} \tag{12}$$

$$x(k) = x(k|k-1) + K(k)[y(k) - Hx(k|k-1)] \tag{13}$$

$$P(k) = [I - K(k)H]P(k|k-1) \tag{14}$$

where $x(k|k-1)$ is the estimate obtained from the optimal estimate at $k-1$. $K(k)$ is the Kalman gain at k . $x(k)$ is the optimal estimate at k . $P(k)$ is the covariance matrix at k , and I is the unit matrix.

Data fusion with KF is the analysis of the sensor data followed by the execution of the KF algorithm to obtain an optimum estimate of the measured values. The best estimate from Equation (13) can be considered the optimal fusion of the observations and estimates consisting of time series signals collected by multiple sensors. The KF-based equation of state for the internal dynamic temperature of the cell can be expressed as Equations (15) and (16):

$$T_G(k) = B_G x_G(k) + v_G(k) \tag{15}$$

$$T_D(k) = B_D x_D(k) + v_D(k) \tag{16}$$

where $T_G(k)$ is the temperature measured using AAS. $T_D(k)$ is the temperature measured using RTD indirect temperature measurement method. B_G is the observation matrix for temperature measurement using AAS. B_D is the observation matrix for temperature measurement using RTD. $v_G(k)$ and $v_D(k)$ are the measurement noises for both methods. According to the core formula of the KF, a relationship given in Equation (17) exists between the two unrelated measurements.

$$T_F = \frac{D_G^{-1}T_G}{D_G^{-1} + D_D^{-1}} + \frac{D_D^{-1}T_D}{D_G^{-1} + D_D^{-1}} \tag{17}$$

where T_F is the temperature obtained after KF fusion, D_G and D_D are the variance of the two measurements, which can be obtained from multiple measurements at a fixed temperature.

To test the effectiveness of the data fusion algorithm that relied on KF, we conducted a simple simulation. During the simulation, the standard deviations of inputs A and B are 0.5 and 0.4, respectively.

Figure 3 shows the KF fusion result, demonstrating the potential temperature signals using KF fusing. The simulate output's standard deviation was reduced to 0.31, indicating the efficacy of the signal fusion algorithm using KF in temperature measurement experiments on cells.

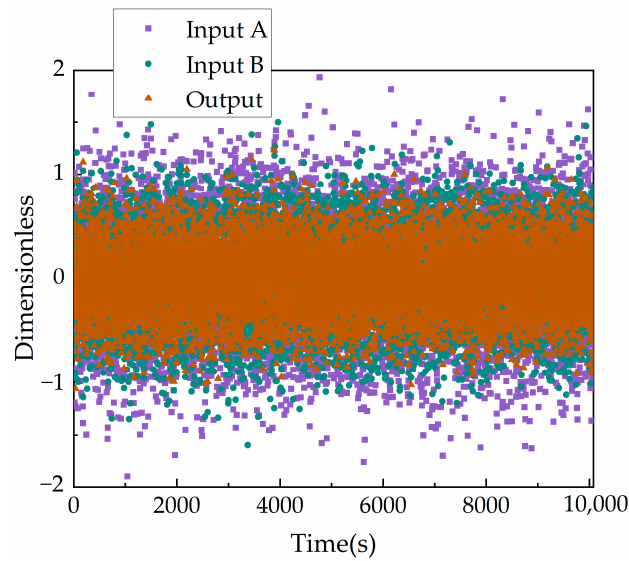


Figure 3. Simulation results of a signal fusion using a KF. It is evident that the variance of the output signal is significantly lower than that of the two input signals.

3. Experimental Setups

The experimental setup consists of a Rb atomic cell, heating oven, electric heating plate, a computer, UniQuanta laser (DFB801-795), two photodetectors (S142C), optical power meter (PM100USB), RTD data acquisition card (M2111) and four RTDs. The schematic diagram of the experimental setup is shown in Figure 4. A 20 mm diameter spherical borosilicate glass cell containing Rb atoms, quenching gas N₂, and buffer gas ⁴He is placed in an oven made of boron nitride. The heating capacity of the oven is provided by two non-magnetic, temperature-controlled electric heating plates with a maximum heating capacity of 473 K. N₂, and ⁴He gases do not produce absorption peaks in the visible light band. In the visible light band, the wavelength of Rb atomic line is at about 794.98 nm. Therefore, the N₂ and ⁴He gases do not affect the experiment. Four RTDs are attached to the outer wall of the cell on both sides of the two ventilation holes. The RTDs are small enough (2 × 5 mm) not to obstruct the transmission of light. This ensures that the RTDs can obtain the most direct temperature of the outer wall of the cell. This also prevents experimental failure due to the malfunction of the small RTDs during experiments. The temperature value measured by the RTD is the average of four individual temperature measurements.

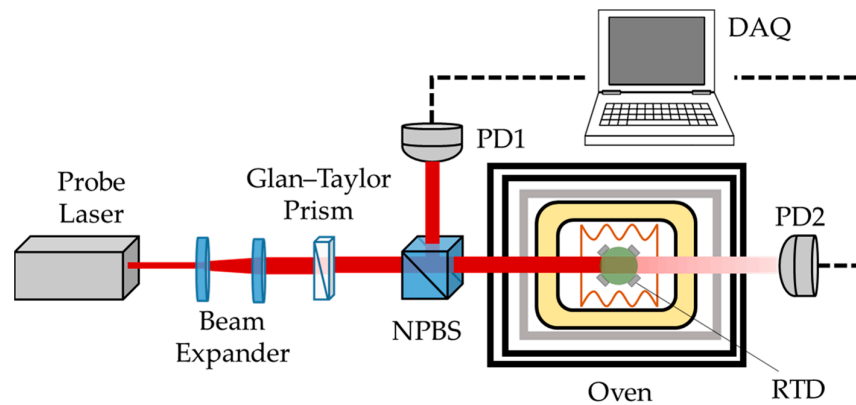


Figure 4. Schematic diagram of the internal dynamic temperature measurement test platform inside the cell.

The heated oven is packed in a non-magnetic tank with two ventilation holes. The detection light enters through a vent on one side of the tank, passes through the cell, and

exits through a vent on the other side. A distributed feedback laser supplies the detection light with a central wavelength of 795 nm. After passing through two plano-convex lenses, the beam is transformed into a linearly polarized beam by using a Glan-Taylor prism as a polarizer. The linearly polarized beam is split in two with a 1:1 ratio using a non-polarization beam splitter (NPBS). One of the beams is directly captured by the photodetector PD1 to detect the intensity of the light. The other beam is captured by the photodetector PD2 after passing through the oven and being absorbed by the Rb atoms to detect the intensity of the light.

Since the cell needs to reach a specific temperature before it can start working, the data for this experiment is recorded from when the temperature of the cell reached 373 K and ended when the external temperature control section of the cell showed a stable temperature of 428 K. A total of 10,800 sampling points were recorded.

Finally, two sets of dynamic internal cell temperatures were obtained for data fusion. Another data set, the external wall's internal dynamic temperature, measured directly, was used for subsequent comparison.

4. Results and Discussion

To measure temperature using AAS, it is necessary to scan DFB lasers near the Rb atomic D1 line to obtain optical depths at different laser frequencies. This is required due to the optical thickness that occurs at higher temperatures and drifts in the DFB laser during usage, which makes it difficult to measure temperature at a fixed frequency. To conduct the experiment, the oven must first be set to a certain temperature. After the oven has reached the desired temperature and has stabilized within a fluctuation range of ± 0.1 K, adjust the wavelength of the DFB laser to scan near the Rb atom's D1 line. It is important to note that the wavelength adjustment step size of the DFB laser varies. Near the D1 line, the step size is 0.08 nm, while it is 0.16 nm, 0.24 nm, and 0.4 nm away from the D1 line. This process was repeated at each working temperature of the cell to calibrate the temperature measurement by AAS.

The OD obtained by AAS varies at different temperatures. This is because, as the cell temperature increases, $I(O)$ gradually decreases while $I(I)$ remains constant. To ensure consistent evaluation of the residual sum of squares (RSS) evaluation indicators for different sets of data after fitting, OD was normalized. RSS is a metric that measures the sum of squares between the actual value OD_i^* and the fitted value \widehat{OD}_i . Usually lower values indicates a better fit. The expression for RSS can be found in Equation (18).

$$RSS = \sum \left(OD_i^* - \widehat{OD}_i \right)^2 \quad (18)$$

Normalization does not affect the data wavelength and therefore does not affect the FWHM obtained after fitting. In this experiment, extreme difference normalization was selected, as shown in Equation (19):

$$OD_i^* = \frac{OD_i - \min OD_i}{\max OD_i - \min OD_i} \quad (19)$$

Temperature measurements by AAS were carried out in 5 K intervals in the operating temperature range of 333–428 K inside the Rb cell. The optical depth as a function of wavelength is obtained over the wavelength range of 794–796 nm in various intervals, as shown in Figure 5, which illustrates the absorption peaks at each sampling temperature.

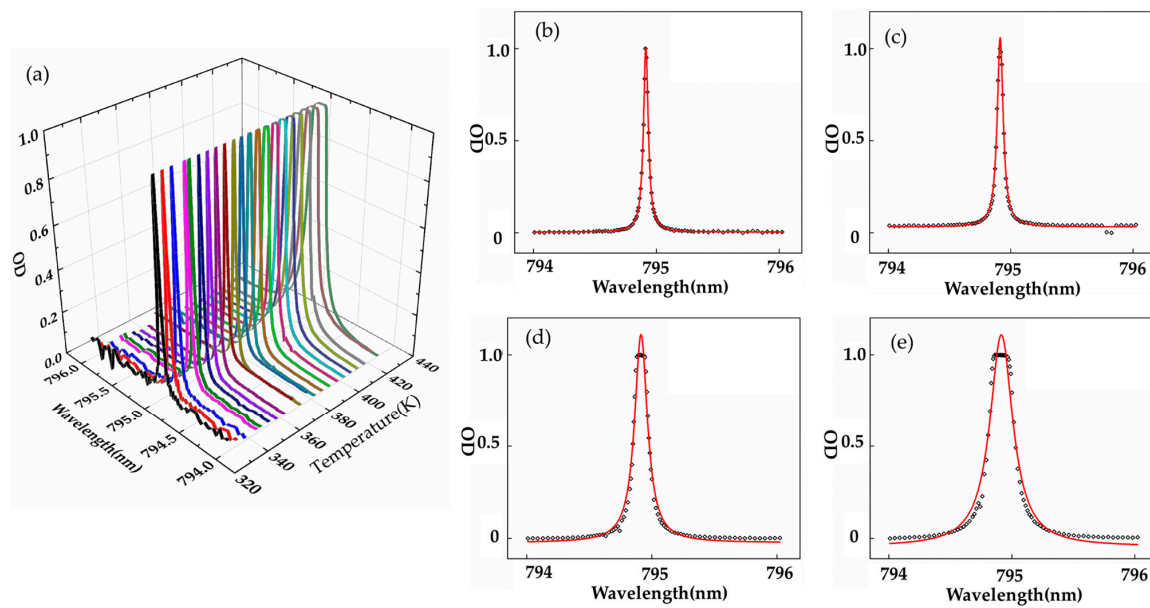


Figure 5. Raw data and fitting results of AAS measurements at each temperature. In items (b–e), the dots represent the measurement results of laser at different wavelengths at a fixed temperature, while the red line represents the fitting curve at the fixed temperature. (a) Absorption peaks at each sampling temperature in the wavelength range from 794–796 nm. (b) Lorentzian fit at 358 K. (c) Lorentzian fit at 378 K. (d) Lorentzian fit at 398 K. (e) Lorentzian fit at 418 K.

The results in Figure 5a indicate that the absorption peak exhibits significant fluctuations on both sides below 333 K, which could be attributed to the incomplete work of the cell. Moreover, Figure 5b–e demonstrates that the absorption peaks become more optically thick as the temperature increases. The waveforms of the absorption peaks also gradually become irregular from the Lorentzian type, resulting in incomplete fitting. An optically thick phenomenon is evident after 398 K.

Table 1 shows that after 11 iterations of fitting with the Lorentz function, the raw data obtained with AAS provides a better fit at low temperatures, but a poorer fit at high temperatures. Inaccuracies in the FWHM obtained by the Lorentz fit can occur due to lower fits, resulting in deviations in calculated temperatures. The high atomic density of the alkali metal vapor at higher temperatures results in complete absorption of the incident beam, ultimately leading to an optically thick absorption peak. In addition, when the laser emitted from the cell is very small, the limited sensitivity of the photodetector resulting in intensity values is unmeasurable, leading to flat peaks. This variance is significant because the indirect RTD measurement method calculates the internal dynamic temperature of the cell using the external temperature of the cell measured by the RTD, and Equation (7) is used in this process. It can seriously affect the accurate measurement of the internal dynamic temperature of the cell.

Table 1. Lorentz function fitting at 358 K, 378 K, 398 K, and 418 K.

Temperature	358 K		378 K		398 K		418 K	
	RSS	R ²						
	0.02576	0.9932	0.01307	0.99729	0.14769	0.98528	0.32702	0.97621

To ensure the accuracy of the data fusion via KF, the oven was cooled to room temperature and reheated to 373 K. Afterwards, both temperature measurement methods were repeated once the temperature stabilized, with fluctuations around ± 0.1 K. The purpose of these measurements was to calculate the variance of the respective methods. The final vari-

ance values are $D_G = 0.0517$ and $D_D = 0.1059$. Subsequently, the data from two temperature measurement methods were fused by KF. The results are displayed in Figure 6.

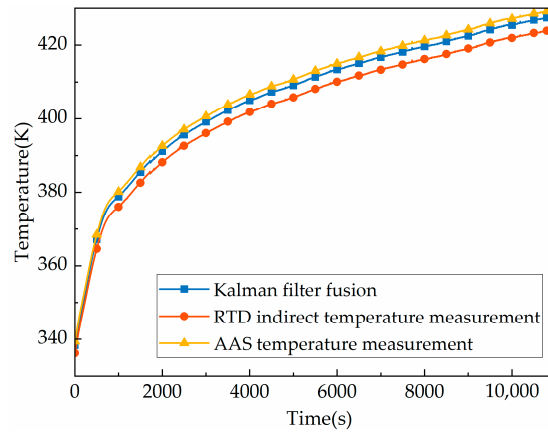


Figure 6. Temperature measurement results using Kalman filter fusion, RTD indirect temperature measurement and AAS temperature measurement.

Figure 6 indicates that the KF fused data is not as high or low as the input data. This is because the output data combines the characteristics of the two input data sets using KF. In this study, the non-magnetic electric heating plates method was used to increase the temperature. However, this method resulted in a sudden temperature rise, most likely due to frequency variation of the plates. This sudden increase in temperature after KF data fusion cannot be eliminated. The consistency of the three curves is high because the measurement data of AAS used RTD measurement data as a reference, resulting in the same trend of the two sets of data. The KF fusion results calculated by Equation (17) also obtained this trend information, thereby ensuring higher consistency.

As shown in Figure 7, the atomic vapor density calculated from the temperature values obtained by fusing the KF data is approximately 37% lower on average than the corresponding values from conventional external wall temperature measurements. This finding is consistent with the results of other studies on calculating atomic vapor density [14,15,35,36]. Furthermore, the density of atomic vapor within the cell becomes progressively more homogeneous as the temperature increases. This is due to the gradual increase of the ratio between the two results. However, after 10,000 s, the temperature increase reaches a state of stagnation. Even when the temperature is stabilized, there is still a 20% difference between the measurement results of the two methods, which may be attributed to the inhomogeneous temperature of the cell.

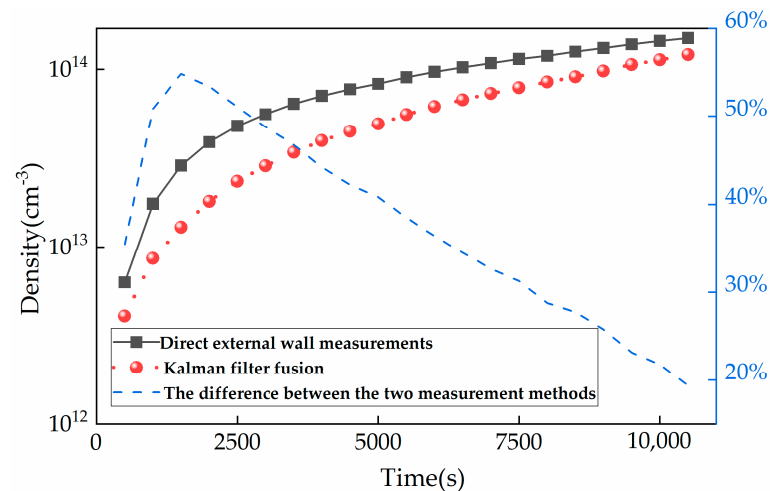


Figure 7. The values of atomic vapor density by KF data fusion and conventional direct gas method.

5. Conclusions

In this study, we used the KF data fusion algorithm to fuse data from RTD and AAS to measure cell temperature more precisely, which is typically difficult. We applied the algorithm to experimental data and observed an improvement in the output result. The experimental results indicate that the proposed KF fusion method can accurately measure the internal dynamic temperature of the cell. In addition, the atomic vapor density calculated by the KF fusion method is approximately 37% lower than the corresponding values directly measured from the outer wall of the cell. This study can be beneficial in improving the accuracy of cell temperature measurement during heating and enhancing the performance of the related atomic precision instrumentation.

However, the low sensitivity of the photodetector used in this study limited the precision of the measurements in the AAS method, specifically for high-temperature measurements. In future work, we could consider using the Faraday modulator [15,37] to address the issue of optical thickness and improve the optical path to enhance the performance of the equipment for the improvement of this study.

Author Contributions: Conceptualization, S.T.; methodology, Y.L.; software, Y.L.; validation, Y.L.; formal analysis, S.T.; investigation, X.L.; resources, Y.L.; data curation, S.T.; writing—original draft preparation, Y.L.; writing—review and editing, J.Z.; visualization, G.Z.; supervision, X.L.; project administration, X.D.; funding acquisition, Y.L. and X.G. All authors have read and agreed to the published version of the manuscript.

Funding: This research was funded by the National Natural Science Foundation of China, grant number 52202456.

Institutional Review Board Statement: Not applicable.

Informed Consent Statement: Not applicable.

Data Availability Statement: Not applicable.

Conflicts of Interest: The authors declare no conflict of interest.

References

1. Zhang, S.W.; Lu, J.X.; Ye, M.; Zhou, Y.; Yin, K.F.; Lu, F.; Yan, Y.G.; Zhai, Y.Y. Optimal Operating Temperature of Miniaturized Optically Pumped Magnetometers. *IEEE Trans. Instrum. Meas.* **2022**, *71*, 7. [CrossRef]
2. Affolderbach, C.; Mileti, G. A compact laser head with high-frequency stability for Rb atomic clocks and optical instrumentation. *Rev. Sci. Instrum.* **2005**, *76*, 073108. [CrossRef]
3. Boto, E.; Meyer, S.S.; Shah, V.; Alem, O.; Knappe, S.; Kruger, P.; Fromhold, T.M.; Lim, M.; Glover, P.M.; Morris, P.G.; et al. A new generation of magnetoencephalography: Room temperature measurements using optically-pumped magnetometers. *NeuroImage* **2017**, *149*, 404–414. [CrossRef] [PubMed]
4. Miao, P.X.; Zheng, W.Q.; Yang, S.Y.; Wu, B.; Cheng, B.; Tu, J.H.; Ke, H.L.; Yang, W.; Wang, J.; Cui, J.Z.; et al. Wide-range and self-locking atomic magnetometer based on free spin precession. *J. Opt. Soc. Am. B* **2019**, *36*, 819–828. [CrossRef]
5. Lu, J.X.; Qian, Z.; Fang, J.C.; Quan, W. Suppression of vapor cell temperature error for spin-exchange-relaxation-free magnetometer. *Rev. Sci. Instrum.* **2015**, *86*, 083103. [CrossRef]
6. Auzinsh, M.; Sargsyan, A.; Tonoyan, A.; Leroy, C.; Momier, R.; Sarkisyan, D.; Papoyan, A. Wide range linear magnetometer based on a sub-microsized K vapor cell. *Appl. Opt.* **2022**, *61*, 5749–5754. [CrossRef]
7. Yan, Y.G.; Lu, J.X.; Zhou, B.Q.; Wang, K.; Liu, Z.A.; Li, X.Y.; Wang, W.Y.; Liu, G. Analysis and Correction of the Crosstalk Effect in a Three-Axis SERF Atomic Magnetometer. *Photonics* **2022**, *9*, 654. [CrossRef]
8. Ma, Y.T.; Qiao, Z.X.; Yu, M.Z.; Wang, Y.B.; Chen, Y.; Luo, G.X.; Yang, P.; Lin, Q.J.; Zhao, L.B.; Zhang, Y.; et al. Single-beam integrated hybrid optical pumping spin exchange relaxation free magnetometer for biomedical applications. *Appl. Phys. Lett.* **2022**, *121*, 114001. [CrossRef]
9. Ma, Y.T.; Chen, Y.; Zhao, L.B.; Yu, M.Z.; Wang, Y.B.; Guo, J.; Yang, P.; Lin, Q.J.; Jiang, Z.D. Accurate determination of alkali atom density based on zero-field magnetic resonance in a single-beam spin-exchange relaxation-free atomic magnetometer. *Meas. Sci. Technol.* **2022**, *33*, 105003. [CrossRef]
10. Ma, Y.N.; Lu, J.X.; Yang, K.; Wang, Z.X.; Wang, Y.G.; Sun, B.W.; Zhai, Y.Y.; Han, B.C. Measuring Spin Polarization of a Spin-Exchange Relaxation-Free Atomic Magnetometer at Extremely Large Optical Depths. *IEEE Trans. Instrum. Meas.* **2022**, *71*, 7007209. [CrossRef]
11. Alcock, C.B.; Itkin, V.P.; Horrigan, M.K. Vapour pressure equations for the metallic elements: 298–2500 K. *Can. Metall. Q.* **1984**, *23*, 309–313. [CrossRef]

12. Lu, J.X.; Wang, J.; Yang, K.; Zhao, J.P.; Quan, W.; Han, B.C.; Ding, M. In-Situ Measurement of Electrical-Heating-Induced Magnetic Field for an Atomic Magnetometer. *Sensors* **2020**, *20*, 1826. [[CrossRef](#)]
13. Shang, H.; Zou, S.; Quan, W.; Zhou, B.; Li, S.; Zhou, W.; Zhao, F. Design of a Measuring Device and Experimental Study into the Relationship between Temperature and the Density of Alkali Metal-Vapor. *Photonics* **2023**, *10*, 112. [[CrossRef](#)]
14. Shao, W.; Wang, G.; Hughes, E.W. Measurement of spin-exchange rate constants between ^{129}Xe and alkali metals. *Phys. Rev. A* **2005**, *72*, 022713. [[CrossRef](#)]
15. Shang, H.; Zhou, B.; Quan, W.; Chi, H.; Fang, J.; Zou, S. Measurement of rubidium vapor number density based on Faraday modulator. *J. Phys. D* **2022**, *55*, 335106. [[CrossRef](#)]
16. Wei, K.; Zhao, T.; Fang, X.; Zhai, Y.; Li, H.; Quan, W. In-situ measurement of the density ratio of K-Rb hybrid vapor cell using spin-exchange collision mixing of the K and Rb light shifts. *Opt. Express* **2019**, *27*, 16169–16183. [[CrossRef](#)]
17. Yin, Y.; Zhou, B.Q.; Wang, Y.X.; Ye, M.; Ning, X.L.; Han, B.C.; Fang, J.C. The influence of modulated magnetic field on light absorption in SERF atomic magnetometer. *Rev. Sci. Instrum.* **2022**, *93*, 6. [[CrossRef](#)]
18. Gravina, R.; Alinia, P.; Ghasemzadeh, H.; Fortino, G. Multi-sensor fusion in body sensor networks: State-of-the-art and research challenges. *Inf. Fusion* **2017**, *35*, 68–80. [[CrossRef](#)]
19. Xiao, F. Evidence combination based on prospect theory for multi-sensor data fusion. *ISA Trans.* **2020**, *106*, 253–261. [[CrossRef](#)]
20. Li, W.; Cui, Z.; Jin, M.; Yu, S.; Wang, X. Dynamic temperature measurement with a dual-thermocouple sensor based on a dual-head one-dimensional convolutional neural network. *Measurement* **2021**, *182*, 109679. [[CrossRef](#)]
21. Apiletti, D.; Baralis, E.; Bruno, G.; Cerquitelli, T. Real-time analysis of physiological data to support medical applications. *IEEE. Trans. Biomed. Eng.* **2009**, *13*, 313–321. [[CrossRef](#)] [[PubMed](#)]
22. Dameshghi, A.; Refan, M.H. Wind turbine gearbox condition monitoring and fault diagnosis based on multi-sensor information fusion of SCADA and DSER-PSO-WRVM method. *Int. J. Model. Simul.* **2019**, *39*, 48–72. [[CrossRef](#)]
23. Gan, Q.; Harris, C.J. Comparison of two measurement fusion methods for Kalman-filter-based multisensor data fusion. *IEEE. Trans. Aerosp. Electron. Syst.* **2001**, *37*, 273–279. [[CrossRef](#)]
24. Slimani, A.; Ribot, P.; Chanthery, E.; Rachedi, N. Fusion of model-based and data-based fault diagnosis approaches. *IFAC-PapersOnLine* **2018**, *51*, 1205–1211. [[CrossRef](#)]
25. Sun, S.L.; Deng, Z.L. Multi-sensor optimal information fusion Kalman filter. *Automatica* **2004**, *40*, 1017–1023. [[CrossRef](#)]
26. Wang, Y.; He, M.; Sun, L.; Wu, D.; Wang, Y.; Qing, X. Weighted adaptive Kalman filtering-based diverse information fusion for hole edge crack monitoring. *Mech. Syst. Signal. Process* **2022**, *167*, 108534. [[CrossRef](#)]
27. Xu, S.; Cheng, J. A new land surface temperature fusion strategy based on cumulative distribution function matching and multiresolution Kalman filtering. *Remote Sens. Environ.* **2021**, *254*, 112256. [[CrossRef](#)]
28. Chen, Y.; Xu, J.; Luo, K.; Xu, S. Multi-temperature and humidity data fusion algorithm based on Kalman filter. *Res. J. Appl. Sci. Eng. Technol.* **2013**, *5*, 2127–2132. [[CrossRef](#)]
29. Kalman, R. A new approach to linear filtering and prediction problems. *J. Basic Eng.* **1960**, *82*, 35–45. [[CrossRef](#)]
30. Măntele, W.; Deniz, E. UV-VIS absorption spectroscopy: Lambert-Beer reloaded. *Spectrochim. Acta A Mol. Biomol. Spectrosc.* **2017**, *173*, 965–968. [[CrossRef](#)]
31. Seltzer, S.J. Developments in Alkali-Metal Atomic Magnetometry. Ph.D. Thesis, Department of Physics, Princeton University, Princeton, NJ, USA, 2008; pp. 238–240.
32. Kluttz, K.A.; Averett, T.D.; Wolin, B.A. Pressure broadening and frequency shift of the D1 and D2 lines of Rb and K in the presence of He3 and N2. *Phys. Rev. A* **2013**, *87*, 032516. [[CrossRef](#)]
33. Zheng, H.J.; Quan, W.; Liu, X.; Chen, Y.; Lu, J.X. Measurement of Atomic Number of Alkali Vapor and Pressure of Buffer Gas Based on Atomic Absorption. *Spectrosc. Spectr. Anal.* **2015**, *35*, 507–511.
34. Guo, Q.; Li, X.; Zhang, N.; Lu, J.; Ma, D.; Li, Z.; Jiang, S. The Space Density Distribution of Alkali Metal Atoms in a SERF Atomic Magnetometer. *IEEE Sens. J.* **2022**, *22*, 6476–6481. [[CrossRef](#)]
35. Chann, B.; Babcock, E.; Anderson, L.W.; Walker, T.G. Measurements of He-3 spin-exchange rates. *Phys. Rev. A* **2002**, *66*, 032703. [[CrossRef](#)]
36. Kadlecak, S.; Anderson, L.W.; Walker, T. Measurement of potassium-potassium spin relaxation cross sections. *Nucl. Instrum. Methods Phys. Res.* **1998**, *402*, 208–211. [[CrossRef](#)]
37. Shang, H.N.; Quan, W.; Chen, Y.; Li, Y.; Li, H. The Measuring Method of Atomic Polarization of Alkali Metal Vapor Based on Optical Rotation and the Analysis of the Influence Factors. *Spectrosc. Spectr. Anal.* **2016**, *36*, 305–309.

Disclaimer/Publisher's Note: The statements, opinions and data contained in all publications are solely those of the individual author(s) and contributor(s) and not of MDPI and/or the editor(s). MDPI and/or the editor(s) disclaim responsibility for any injury to people or property resulting from any ideas, methods, instructions or products referred to in the content.